OPTICA

Label-free multimodal polarization-sensitive optical microscope for multiparametric quantitative characterization of collagen

LINGXIAO YANG,[1,2] **RISHYASHRING R. IYER,**[1,2] **JANET E. SORRELLS,**[1,3] **ERIC J. CHANEY,**[1] **AND STEPHEN A. BOPPART**[1,2,3,4,5,6,*]

[1]*Beckman Institute for Advanced Science and Technology, University of Illinois Urbana-Champaign, Urbana, Illinois 61801, USA*
[2]*Department of Electrical and Computer Engineering, University of Illinois Urbana-Champaign, Urbana, Illinois 61801, USA*
[3]*Department of Bioengineering, University of Illinois Urbana-Champaign, Urbana, Illinois 61801, USA*
[4]*NIH/NIBIB Center for Label-Free Imaging and Multiscale Biophotonics, University of Illinois Urbana-Champaign, Urbana, Illinois 61801, USA*
[5]*Cancer Center at Illinois, University of Illinois Urbana-Champaign, Urbana, Illinois 61801, USA*
[6]*Interdisciplinary Health Sciences Institute, University of Illinois Urbana-Champaign, Urbana, Illinois 61801, USA*
*boppart@illinois.edu

Collagen is an essential component of biological tissues with a variety of subtypes. To be able to capture these subtypes, fully exploit the polarization-sensitive light-collagen interactions, and provide comprehensive information of collagen, we integrated polarization-sensitive second-harmonic generation (PSHG) microscopy, polarization-sensitive optical coherence microscopy (PSOCM), and two-photon fluorescence lifetime imaging microscopy into a single-source multimodal system in a simultaneous and spatially co-registered configuration. PSOCM information is used in the PSHG numerical model to enable accurate PSHG analysis of unsectioned fresh tissue. This polarization-sensitive multimodal system provides quantitative multiparametric characterization of collagen and facilitates the fundamental understanding of collagen in the unperturbed tissue microenvironment, which can enable future studies into the role of collagen in various diseases. © 2024 Optica Publishing Group under the terms of the Optica Open Access Publishing Agreement

1. INTRODUCTION

Collagen is known as the main structural protein in the extracellular matrix (ECM) and has a variety of subtypes with different properties and functionalities [1–3]. In the ECM, the basement membrane is composed of type IV collagen while the interstitial matrix mainly contains collagen types I, III, and V [1–3]. Although type I is the most abundant collagen in the human body, it is also important to recognize the roles and characteristics of other subtypes. For example, type II collagen is abundant in cartilage, and its degradation has been found to be associated with osteoarthritis [4]. Type III collagen is essential for type I fibrillogenesis, especially in the cardiovascular system and skin [5]. Type IV collagen is primarily found in the basement membrane, and its disruption is a critical indicator for tumor progression [3]. Visualization of collagen subtypes can facilitate the understanding of their roles in the biological tissue and potentially benefit early diagnosis of diseases. Optical techniques stand out among common imaging methods because of their spatial resolution and accessibility. Label-free optical imaging has been increasingly prominent because it removes the need to inject exogenous contrast agents, making it a non-perturbative and non-toxic tool that can be used on fresh tissue specimens or even *in vivo*.

Various optical imaging techniques have been used to visualize and characterize collagen in biological tissues based on different light-collagen interaction mechanisms. For instance, conventional confocal reflection microscopy [6,7] has been used to track collagen fibrillogenesis *in vitro* [6] and corneal collagen crosslinking *in vivo* [7]. Optical coherence tomography and microscopy (OCT and OCM) are well-known label-free imaging techniques based on light scattering [8–10], and collagen fibers are identified as strong scatterers due to the relatively high refractive index [10]. Polarized light microscopy is a traditional method to examine collagen microstructures based on birefringence, although collagen-specific stains are often used in some clinical settings [11–13]. More recently, with the development of nonlinear optical imaging methods, second-harmonic generation (SHG) microscopy has been a prevalent imaging tool for studying collagen in various parts of the body [14–16] and has been recognized as a potential biomarker for predicting tumor progression [17–20]. Another widely used multiphoton microscopy (MPM) technique in the field of biomedicine is two-photon autofluorescence (2PAF), which is mostly focused on examining autofluorescence from three essential metabolic cofactors, namely NADH, NADPH, and FAD [21–23]. However, collagen also generates autofluorescence [24], and there have been a few demonstrations with two-photon excited autofluorescence of

collagen [25,26]. Autofluorescence lifetime has also been a valuable tool for differentiating collagen subtypes [26]. Vibrational spectroscopy techniques were also used to reveal biochemical signatures of collagen, such as Raman and sum frequency generation [27–29].

Due to the birefringent nature of collagen, polarization-sensitive imaging techniques can reveal more biomolecular and biophysical information other than morphological features. For example, polarization-sensitive OCT has been used to measure linear birefringence (from measuring phase retardation) and the fast birefringent axis (also called optical axis) in biological tissue, which is further used to differentiate diseased versus normal biological tissue in many areas of applications, such as breast cancer, skin diseases, and osteoarthritis [30–34]. Polarization-sensitive SHG (PSHG) is a recently developed technique that provides information about collagen fiber angle in the focal plane, SHG-defined anisotropy parameter, and estimated helix angle [35–44]. There have been thorough theoretical derivations of the PSHG numerical models for collagen [35–38,40,44] and many experimental demonstrations of the PSHG of collagen in biological tissues [39–44]. Most recently, a few studies focused on the clinical applications of PSHG [41–43]. However, common sample preparation involves the thin sectioning of frozen or fixed tissue. This is mainly because tissue birefringence and scattering are neglected in

the existing PSHG numerical model [38] since this cannot be measured with SHG alone. Though the effect of birefringence has been identified previously, there has not been an experimental solution other than assuming an empirical refractive index of collagen-rich tissue in an epi-detection configuration.

In recent decades, various advances in SHG technologies have been made toward a more comprehensive and quantitative tumor-associated collagen signature (TACS) [18–20]. SHG has also been included in many multimodal multiphoton imaging systems for collagen contrasts [23,45–47]. However, it is known that type IV collagen, which constitutes the basement membrane, cannot produce SHG signals due to its molecular structure and distribution [26]. Therefore, to be able to provide a more comprehensive understanding of collagen in tissue, other imaging modalities are needed.

Here we propose and demonstrate a novel multimodal polarimetric imaging system combining polarization-sensitive SHG, polarization-sensitive OCM, and two-channel 2PAF lifetime imaging (PP2) with a single laser source. The multiparametric PP2 system can provide simultaneous and co-registered measurements of collagen signatures as well as surrounding tissue elements such as different types of cells, lipids, and elastin. Figure 1 shows a conceptual overview of the multiparametric, and multiscale
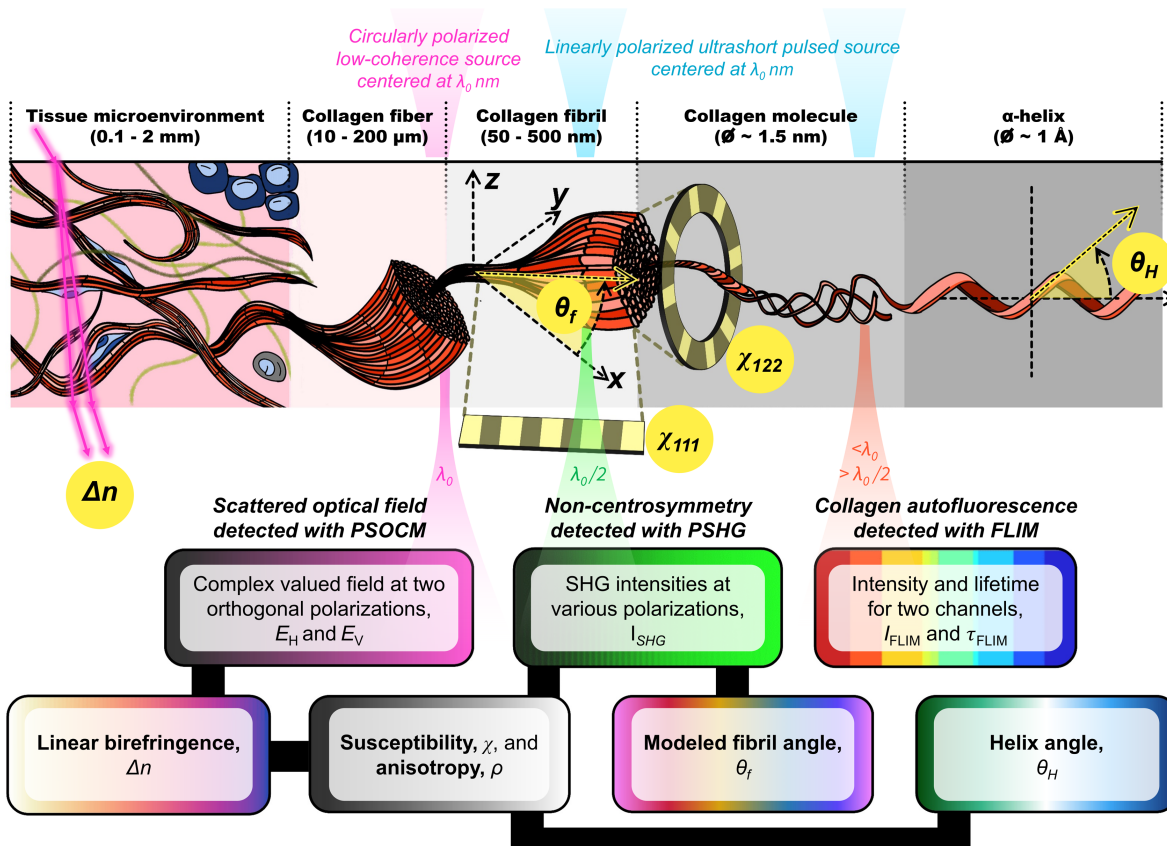
Fig. 1. Multiparametric polarization-sensitive optical characterization of collagen at different scales. A collagen hierarchy is shown in the top panel. At the tissue level, linear birefringence of the material causes refracted light of two polarizations to travel at different angles. At the scale of collagen fiber bundles and fibrils, scattering and SHG processes occur. The orientation of the fibrils along the coordinate axis is called the fibril angle. PSOCM detects scattered light fields at two polarizations, which are used to calculate linear birefringence. Collagen molecules can be excited and generate autofluorescence. Both fluorescence intensity and lifetime can be detected using a time-tagged method. A single helix, though not resolvable by optical microscopy, twists along its axis with an angle, called the helix angle. By modeling the SHG response of collagen fibril to variations of excitation polarizations and experimentally measuring the linear birefringence from PSOCM, one can retrieve the fibril angle, calculate the SHG-defined anisotropy parameter from the ratio of the nonlinear susceptibilities along two axes, and estimate the helix angle. The color schemes for each parameter in the text boxes are consistent with the color scales used for the heatmaps for these parameters in the later figures.

quantification and characterization of collagen enabled by this work. We made use of different light-collagen interactions at different scales from the tissue level to the collagen fiber and fibril levels and to the molecular and atomic levels. PSOCM detects the scattering signals from the collagen on the micron and sub-micron scales and measures the bulk birefringence (in the 100 µm scale). PSHG detects the non-centrosymmetries, and a cylindrical model of collagen is used to define anisotropy and estimate fiber in-plane angles and the helix angle. The linear birefringence measured by PSOCM is used in the numerical model to enhance accuracy. At the molecular level, collagen autofluorescence (together with signals from other autofluorophores) and its lifetime are detected by 2PFLIM.

In this paper, we first imaged collagen gels of type I-IV to show that different subtypes produced distinct optical signatures through PSOCM, SHG, and 2PFLIM. Second, we demonstrated that an upgraded PSHG numerical model including tissue birefringence measured by PSOCM gave accurate and repeatable analysis results in fresh rat tendon, 30 µm below the surface. Last, we imaged rodent outer ears that have depth-dependent collagen subtype distributions and showed that the PP2 system can provide a multidimensional characterization of collagen and thus facilitate a greater understanding of collagen and subtypes in the tissue microenvironment.

2. MATERIALS AND METHODS

A. Polarization-Sensitive Multimodal Microscope

The PP2 platform (Fig. 2) sources light from a titanium-sapphire laser (InsightX3+, Spectra-Physics) at 760 nm. The MPM excitation path (blue) and the OCM path (green) were split after a half-wave plate (HWP), and a polarization beam splitter (PBS) was used for power ratio tunability. Around 700 mW was used to pump a photonic crystal fiber (PCF) (LMA-PM-5, Thorlabs Inc.) to generate a broadband continuum for OCM. The other part of the beam was attenuated by a HWP and a Glan-Thompson polarizer (GTH5-A, Thorlabs Inc.), and it was focused through a pinhole to filter out the higher-order spatial modes. Following this, the beam was then collimated. These optical elements were omitted

from the setup diagram for brevity. An HWP (highlighted in red in Fig. 2) was placed in the MPM excitation path before combining it with the OCM path to control the excitation polarization angles. Elements in the MPM path after this HWP were not polarizing. At 760 nm, the bandwidth at the output of the PCF was 40 nm (at full-width half-maximum), corresponding to an axial resolution of approximately 6 µm in air. The PCF output was collimated with a parabolic mirror and temporally dispersed by passing through 10 cm of SF11 glass. The OCM source was circularly polarized using a linear polarizer (LP) and a quarter-wave plate (QWP) and split into sample and reference beams. The OCM sample arm recombined with the MPM excitation beam and traveled co-linearly through a pair of galvanometer mirrors (6230 H, Cambridge Technology) separated by a telescope for telecentric scanning, ensuring a flat focal plane. Both beams were translated with a scan and tube lens in a 4f configuration and focused on the sample through an objective lens (XLPLN25XWMP2, Olympus Corporation) for imaging in the epi-direction.

Samples were placed on a 3D motorized stage (FTP-2000, Applied Scientific Instrumentation) under custom-written LabVIEW software control. In the MPM detection arm, a dichroic mirror (DM1, FF665-Di01, Semrock) separated the MPM signals from the excitation light. Two hybrid photodetectors (HPD1 and HPD2, R10467U-40, Hamamatsu) and an analog output photomultiplier (PMT, H10721-210, Hamamatsu) were used for signal detection at different spectral bands (Ch1, 390-506 nm; Ch2, 506-665 nm) with swappable DMs (DM2, FF506-Di03, Semrock; DM3, FF390Di01, Semrock). Bandpass filters for each channel were optional and can be easily changed through filter wheels. No filters were used before the HPDs, and one filter (FF02-379/34, Semrock) was used before the PMT unless stated otherwise. Details about the HPD signal amplification, high-speed digitization, and real-time processing can be found in our previous publications [48–50]. The PMT was connected to a USB external high-speed photon counting module (MCPC618, Vertilon). For OCM, the reference beam contained a polarization-dependent delay loop where the optical path lengths differed for each polarization state. The dispersion mismatch between the reference and the sample arm was compensated optically with glass blocks
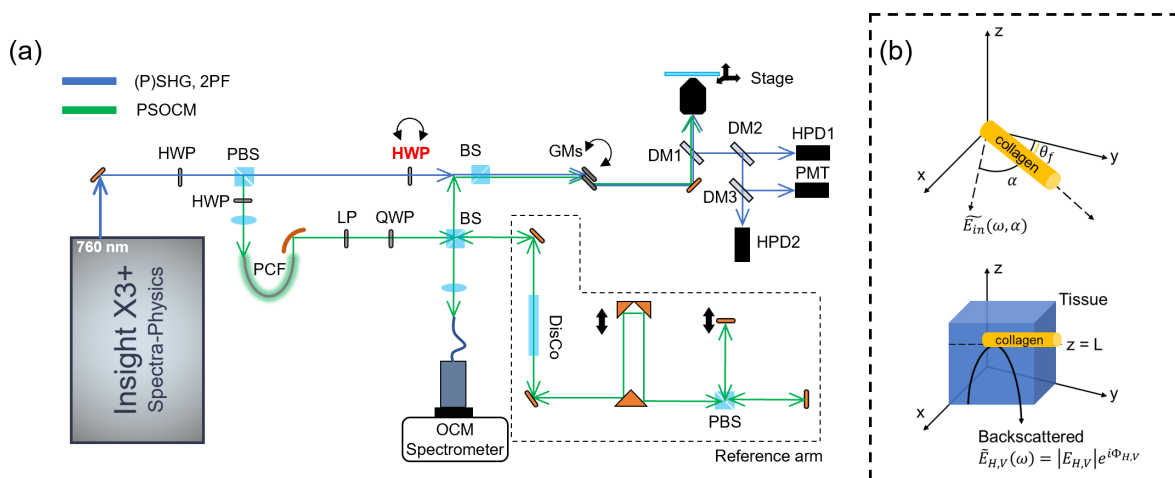
Fig. 2. PP2 system combining PSHG, PSOCM, and 2-channel 2PFLIM with a single laser source. (a) Optical setup schematic. (b) Diagrams to illustrate the spatial relations between the collagen fiber (modeled as a cylinder), and the incident electric field for PSHG (top) and PSOCM (bottom). HWP, half-wave-plate; PBS, polarization-sensitive beamsplitter; PCF, photonic crystal fiber; LP, linear polarizer; QWP, quarter waveplate; BS, beamsplitter; GM, galvanometer mirror; DM, dichroic mirror; PMT, photomultiplier tube; HPD hybrid photodetector; DisCo, dispersion compensator. All the beam size adjustment elements and power attenuating elements were omitted for brevity.

and slides (BK7 and SF11) of approximate equivalent thickness in the reference arms and computationally in post-processing. The polarization-multiplexed signal was detected using a single spectrometer (Cobra-S 800, Wasatch Photonics) line scan camera (OctoPlus, Teledyne Inc.) connected to a frame grabber (PCIe 1433, National Instruments Corp). All OCM intensities of biological samples at the two polarizations were normalized to the images of a clean glass surface. The MPM excitation beam at the sample plane was measured to have a pulse width of around 200 fs and 15–20 mW of average power at 760 nm center wavelength. The OCM incident power on the sample was about 5 mW.

B. PSHG Numerical Model with PSOCM Birefringence Measurements

The PSHG numerical model used in this work was based on the model described by Schanne-Klein and collaborators [36,37]. We adopted the most common cylindrical modeling of collagen fibers [coordinates shown in Fig. 2(b)] and assumed Kleinman symmetry so only two elements in the second-order susceptibility tensor are independent. The SHG intensity varies with excitation polarization angle α:

$$I_{\text{SHG}}(x, y, \alpha) = I_0(|\chi_{111}e^{i\Delta\phi}\cos^2(\alpha - \theta_f) + \chi_{122}\sin^2(\alpha - \theta_f)|^2$$

$$+ |\chi_{122}\sin(2\alpha - 2\theta_f)|^2),$$

where θ_f is the in-plane angle of the collagen fiber. In the subscripts of susceptibility χ, the number 1 denotes the axis along the cylinder, whereas 2 denotes the radial axis orthogonal to 1. The term $\Delta\phi$ denotes the phase retardation due to birefringence. The birefringence Δn at the imaging plane at a certain depth L is given by the co-registered PSOCM, which measured the back-scattered complex electric fields at two polarizations (E_H, E_V) as illustrated in the bottom diagram in Fig. 2(b):

$$\Delta n = \frac{\lambda_0}{2\pi L}\tan^{-1}\left(\frac{|E_H|}{|E_V|}\right),$$

where λ_0 is the center wavelength (760 nm in this work). One can compute the phase retardation due to birefringence by

$$\Delta\phi = \frac{2\pi \Delta n L}{\lambda_0}.$$

A fast Fourier transform (FT) method [44] was used to compute the θ_f and other quantities, namely the SHG-anisotropy parameter ρ and estimated helix angle θ_H:

$$\rho = \frac{\chi_{111}}{\chi_{122}}, \; \theta_H \approx \cos^{-1}\left(\sqrt{\frac{\rho}{\rho + 2}}\right).$$

C. Data Acquisition and Processing

Data of all modalities were acquired using custom-written LabVIEW software based on what has been described in Ref. [45]. Unless otherwise specified, each 2D *en face* image was 400×400 pixels ($128\,\mu\text{m} \times 128\,\mu\text{m}$). Each pixel contained responses from 1024 laser pulses, which corresponds to a pixel-dwell time of 12.8 µs. The line-scan rate was set to 80 Hz for all modalities. For OCM, 2048 pixels were acquired along the spectral axis for each A-scan. The post-processing of OCM data was similar

to our previous work [45], which involves dispersion compensation, spectral shaping, k-space resampling, and inverse FT. OCM mean intensity images were the averaged OCM intensities of the two polarization states. Birefringence was calculated using the equation specified in the previous section. For 2PFLIM, the signals from the HPDs were processed in the same way as described in our previous publications [48–50]. In brief, emitted fluorescence was directed to two HPDs, each detecting a different spectral range (390–506 nm and 506–665 nm). These channels were chosen to separate the autofluorescence from NAD(P)H and FAD for potential cell metabolism analysis. The analog output of the HPD was amplified using a high-speed transimpedance amplifier (Femto HSA-X-2-20), and the voltage was digitized using a high-speed digitizer at 5 GS/s (ADQ7WB, Teledyne SP Devices). Photon counts were discriminated using the single- and multi-photon peak event detection (SPEED) algorithm [49], which has been shown to produce accurate results for fluorescence intensity and lifetime for signals at up to photon rates up to 223% [50]. For this study, photon rates were generally in the range of 5–50%, and data acquired above 200% photon rate were discarded. Fluorescence intensity and lifetime were estimated in real-time via GPU accelerated processing [48] to monitor performance during data acquisition; the fluorescence decay curve was additionally saved to enable deconvolution and spatial binning in postprocessing. The mean fluorescence lifetime was estimated using the mean phase lifetime from phasor analysis: $\tau_{\text{mean}} = \frac{s}{g\omega}$ [51], where g is the normalized cosine component, s is the normalized sine component, and ω is the laser repetition angular frequency ($2\pi \times 80$ MHz). Deconvolution with the system impulse response function (IRF, shown in Supplement 1, Fig. S1) was performed during the phasor analysis. More details on the FLIM processing can be found in Supplement 1 and Fig. S1. Mean-lifetime images were displayed after 3×3 median filtering with a linear colormap overlaid on intensity. All SHG-derived parameters and OCM-derived parameters were displayed after median filtering and with a transparency map generated using the intensity map normalized by the mean intensity of the whole frame. All histograms were generated after intensity thresholding and without median filtering. All post-processing of the modalities was performed through MATLAB 2022b (MathWorks).

D. Collagen Gel Preparations and Imaging

Collagen gels for type I, II, and III collagen were made from the following commercially available solutions: rat collagen I, 5 mg/mL (3440-005-01, Cultrex), collagen II from bovine, 3 mg/mL (CL354257-1, Corning), and type III collagen from human placenta, 1 mg/mL (5021, Advanced Biomatrix). The purity for type I and II collagen was over 95%, but the purchased type III solution contained about 15% type I. For collagen type IV, we dissolved purified powder derived from human placenta (C7521-5MG, Sigma-Aldrich) in 0.5 M acetic acid. For the acid-diluted collagen solutions, a mixture of 1 N NaOH, 10x Phosphate Buffered Saline (Fisher Scientific), and deionized water was added to neutralize the acidity while maintaining a final pH of 7.4. The neutralization was performed with all components kept on ice and inside a biosafety cabinet to ensure optimal airflow. The gels were formed under room temperature for 2 h initially and then transferred to an incubator kept at 37°C, 100% humidity, and 5% CO_2 to prevent pH imbalances or dehydration. Type I, II, and IV collagen gels had a concentration of about 2 mg/mL, whereas type II gels were made

into 0.9 mg/mL due to the lower concentration of commercially available solutions. PP2 imaging of collagen gels was performed with 760 nm excitation. MPM detection used the HPD1 without DM2 so that all signals below 665 nm containing both SHG and 2PAF responses of collagen were collected.

E. SEM Preparation and Imaging

The collagen gels were fixed overnight after PP2 imaging with 2.0% paraformaldehyde and 2.5% glutaraldehyde in 0.1 M Na-Cacodylate buffer, pH 7.4 (buffer). The solutions used were all of electron microscopy grade. The samples were rinsed using the buffer solution on a shaker table for 10 min and went through a multi-step dehydration process. During the dehydration process, the samples were rinsed with 37%, 67%, 95% ethanol for 10 min each time, and 100% ethanol for 10 min three times. Hexamethyldisilane was then used to replace ethanol, and the samples were left overnight in a desiccator for further dehydration. The dry samples were mounted on metal stubs using sticky carbon tape and sputter coated with a gold-palladium alloy. The samples were then imaged using a commercial SEM system (Quanta FEG 450, FEI).

F. Rodent Tissue Sample Extraction and Imaging

The rat tail tendon, rat outer ear, and mouse outer ear samples were extracted postmortem, following euthanasia by CO_2 overdose. All tissue specimens were surgically resected and placed in an imaging dish containing cold saline. The outer skin layers of the rat ear were removed to expose the muscle and cartilage layers. All animal procedures were conducted under a protocol approved by the Institutional Animal Care and Use Committee (IACUC) of the University of Illinois Urbana-Champaign.

G. H&E Staining and Histology

Formalin-fixed, paraffin-embedded tissues were sectioned at 5 μm on a microtome (Leica) and stained with hematoxylin and eosin for microscopic observations. Microscope slides were digitized using a slide scanner (Nanozoomer 2.0 RV w/fluorescence, Hamamatsu).

3. RESULTS

A. PSOCM and 2PFLIM of Collagen Gels

We imaged four major types of collagens in their gel forms with the PP2 system. Figure 3 shows the representative images of these collagen gels. OCM intensity images in magenta show the scattered signals from about 10–15 μm deep in the gels. The morphology of each collagen gel sample was also confirmed under a scanning electron microscope (SEM). Type I fibrils in gels appear rope-like and form a dense network. Both type II and III appear to be straight segments of fibrils in OCM images, but type III is thinner in diameter and produces weaker scattering signals. The birefringence images show that all four types of collagens are birefringent, and histograms indicate that type I collagen produces relatively higher birefringence. Note that the birefringence distributions in type II and III are broader than that in type I and IV due to the higher degree of heterogeneity in the gels and the computational inaccuracies from a weaker scattering signal from the nearly transparent gels compared to biological tissues.

MPM images in green show similar structures of collagen compared to OCM. To be able to differentiate the contribution of SHG in all MPM signals, we collected MPM (potentially containing both SHG and 2PAF) signals in one detector for a broad spectral range and quantified lifetime distributions. Since deconvolution using the system IRF was performed, the SHG component should have a zero mean lifetime. As seen in Fig. 3, the lifetime measured from type I collagen gel has a strong low-lifetime distribution, and the mean value was calculated at around 0.25 ns. This indicates
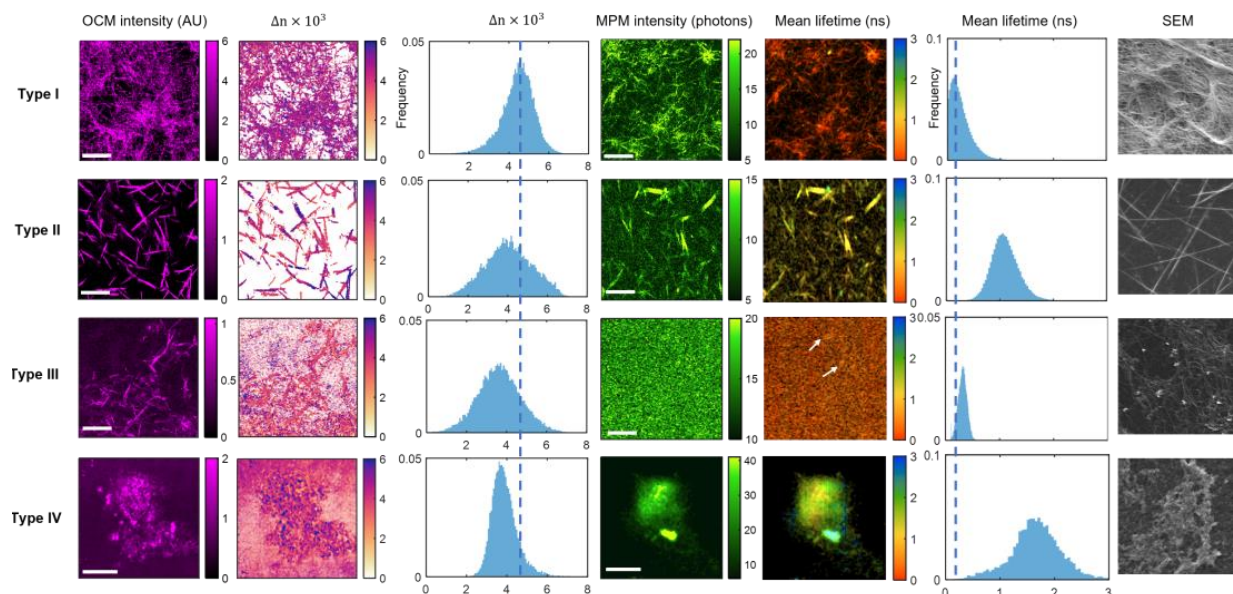
Fig. 3. PSOCM-MPM of different types of collagens in pure gel form. OCM intensity (magenta) and MPM intensity (green) images show that different types of collagens in their pure gel forms have different morphologies, which were confirmed by the SEM images (greyscale) of the same gel samples (not the same FOV). Birefringence Δn was scaled up by 10^3 for display purposes only. The blue dashed line across the birefringence histograms was placed at $\Delta n \times 10^3 = 4.5$. The dashed line across mean lifetime histograms was placed at 0.25 ns for comparison. White arrows pointed to type III collagen regions in the MPM mean lifetime image. All scale bars represent 25 μm. SEM FOVs are 50×50 μm^2.
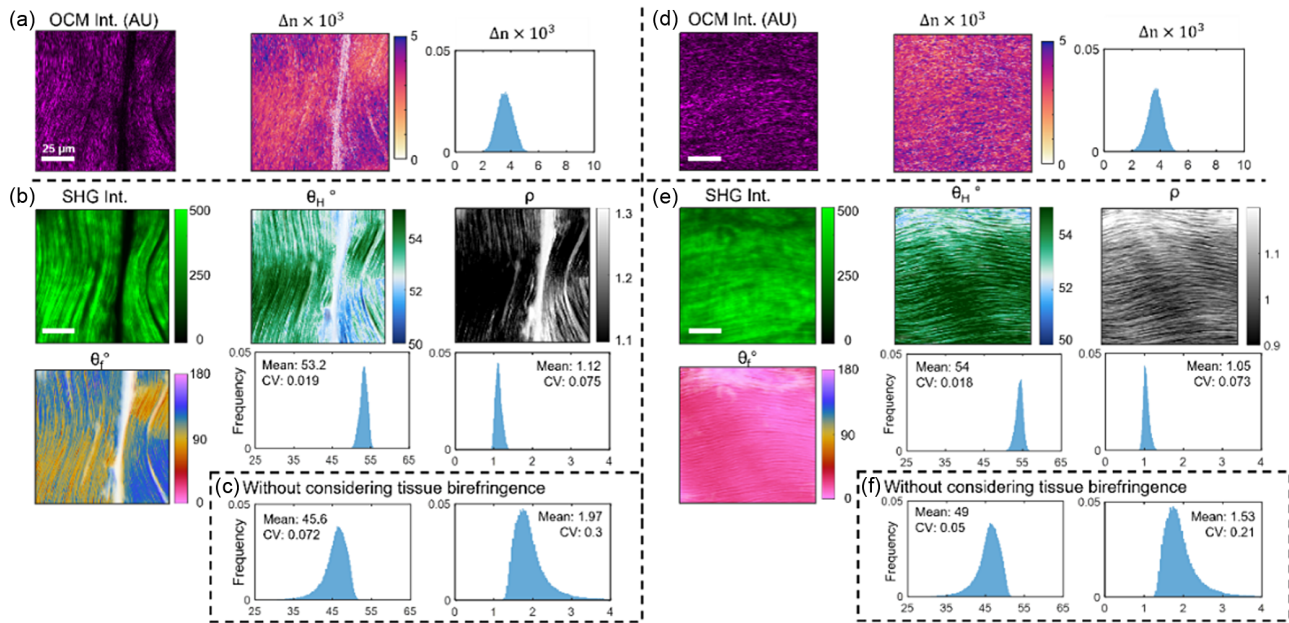
Fig. 4. PSOCM-PSHG of fresh rat tendon. Type I collagen fibers were aligned at two apparent orientations (a)-(c), (b)–(f). (a), (d) PSOCM measurements of tissue birefringence (Δn). (b), (e) PSHG measurements of fiber in-plane angles (θ_f), estimated helix angles (θ_H), and SHG-anisotropy parameters (ρ) with considering tissue birefringence in the numerical model. OCM intensity images were the mean intensities at two polarizations. SHG intensity images were obtained by averaging SHG intensities at excitation polarizations tuned from 0°–180° in intervals of 10°. All scale bars represent 25 µm. CV, coefficient of variance.

that type I collagen produces both SHG and 2PAF with 760 nm excitation, but SHG dominates. A similar distribution was found in type III collagen gel with a slightly higher mean value of the lifetime distribution at 0.32 ns. The MPM images of type III collagen did not appear to have great contrast for individual fibers or fibrillar structures, even though the mean intensity level is comparable to the other types of collagen. This is because the type III collagen is reticular and forms a fine woven network as seen in the SEM image on the right-most column. Each fibril has a size of tens of nanometers, which is far below optical resolution. In the lifetime images, there are still some distinguishable structures, as pointed out by the white arrows. Both type II and type IV have relatively longer lifetimes, with mean values around 1 ns and 1.4 ns, respectively, suggesting that the SHG signals are weak or negligible. We also observed separations in the phasor analyses (Supplement 1, Fig. S2).

B. PSOCM and PSHG of Rat Tendon

Tendons are mostly made of type I collagen, and the fibrils are often highly directionally aligned [2]. We imaged a fresh piece of rat tendon at around 30 µm below the surface to show that integrating the tissue birefringence measured by PSOCM into the PSHG numerical model for collagen fibrils yields a more accurate estimation of the anisotropy and helix angles. The SHG intensities shown in Fig. 4 were spectrally filtered to exclude the tissue autofluorescence. Figure 4 shows results from two FOVs that had two different overall fibril orientations. In Figs. 4(a)–4(c) the fibrils are mostly aligned vertically, whereas in Figs. 4(d)–4(f) they are horizontally oriented with respect to our imaging axis, which can be confirmed in the intensity images of both OCM and SHG. Since the fibrils are highly aligned, the retrieved fiber in-plane angle (θ_f) is close to the apparent orientation angle, as seen in Figs. 4(b) and 4(e). Both FOVs had birefringence values around 3.6×10^{-3} measured

by PSOCM. With the numerical model including tissue birefringence, the retrieved helix angle (θ_H) for this tendon had a mean value of about 53°–54° with CV less than 2%, which matches well with existing biomolecular models of collagen [35,40]. In comparison, without considering the tissue birefringence, the mean helix angle for the two FOVs varied from 45° [Fig. 4(c)] to 49° [Fig. 4(f)] and the CVs were over 5%. Consistent results for both apparent orientations validate that the retrieved parameters are not an artifact of imaging configuration.

C. Multiparametric Quantitative Characterization of Collagen in Unsectioned and Unstained Tissue

Rodent outer ears contain different layers of distinct structures. The epidermal skin is primarily made of a variety of cells, while the dermal skin contains primarily type I (and some type III) collagen [52]. The two layers are separated by a thin collagen type IV layer, which is known as the basement membrane [53]. Under the dermal layer, there is a layer of cartilage that is composed of type II collagen [54]. The hypodermis in the ear contains striated muscle, which also contains type I collagen [55]. Figure 5 contains PP2 imaging results from two rodent outer ears. Each row summarizes results from FOV images from the epidermis layer to the hypodermis muscle layer. FOV1–FOV4 were from a mouse, and FOV5 was from a rat. The imaging depth was limited to around 100 µm inside the tissue, which was not sufficiently deep to reach hypodermis from the skin surface for either the mouse or the rat ear. The rat's outer ear was thick enough to surgically remove the superficial skin layers and expose the muscle layer. Columns from left to right show the results of fluorescence lifetime signals collected in two hybrid photodetectors (τ_{ch1}, τ_{ch2}), SHG normalized intensities (green, averaged over all excitation polarizations), OCM normalized intensities (magenta, averaged over two polarizations), tissue birefringence at the imaged plane (Δn), in-plane fiber angle (θ_f),
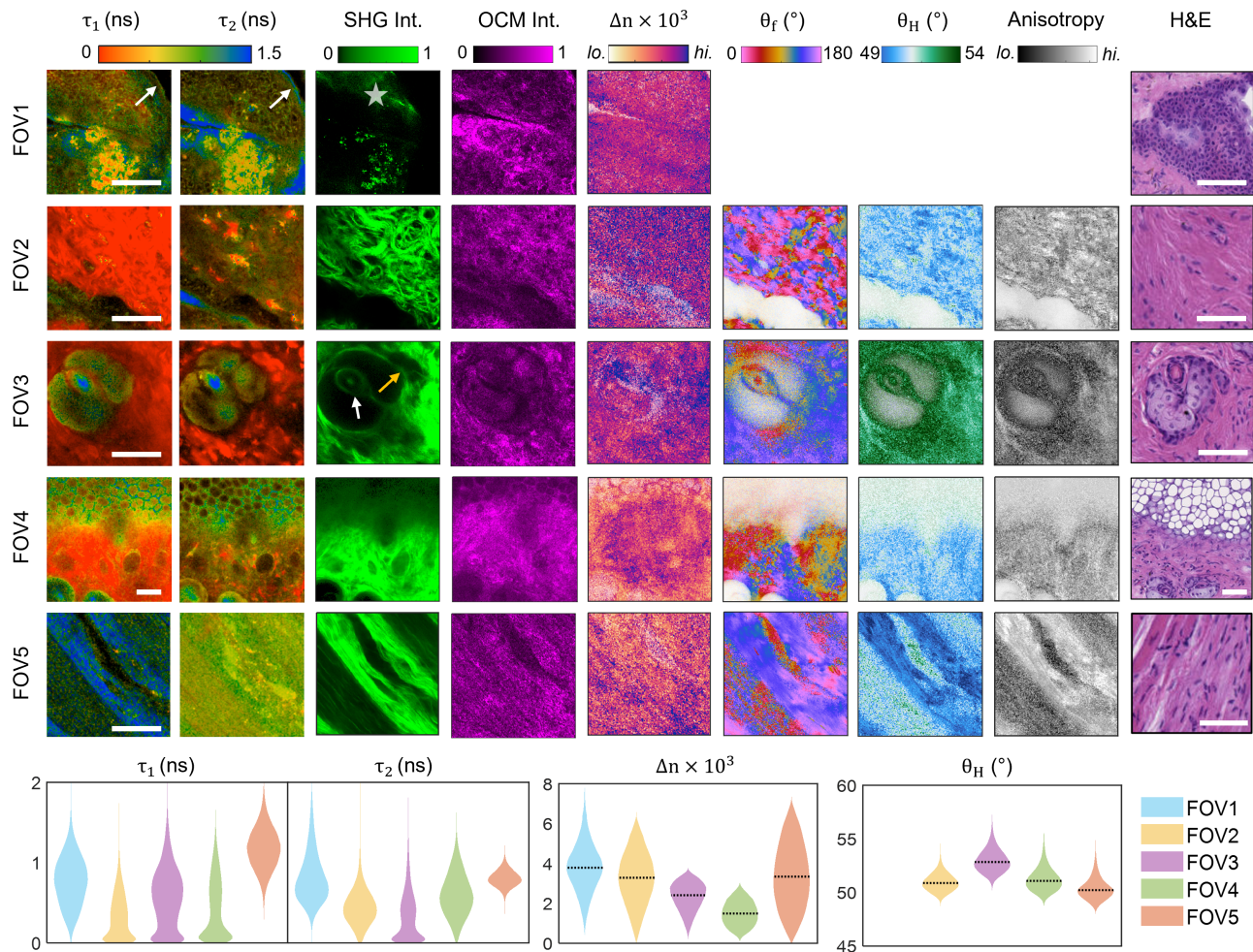
Fig. 5. PP2 imaging of rodent outer ears at different depths revealing different optical signatures of collagen and their microenvironments. Brightness represents MPM intensities in lifetime images. FOV1, the transition from the epidermis (white arrows indicate membrane-like structure) to the dermis (star region). Because the SHG intensity was too weak to perform PSHG analysis, θ_f, θ_H, and anisotropy images are blank. FOV2, the dermis. FOV3, a hair follicle (the white arrow indicates the inner root sheath, and the yellow arrow indicates the dermal sheath) in the dermis layer. FOV4, the transition from the dermis to cartilage (porous structures at the top of the image). FOV5, muscle layer underneath dermal layer. FOV1-4 were acquired from the same piece of mouse ear and were imaged from the same side, at depths of 20 µm, 25 µm, 50 µm, and 60 µm, respectively. FOV5 was acquired from a rat ear and was imaged 20 µm into the subcutaneous region. All scale bars represent 25 µm. All lifetime images were displayed after 3×3 median filtering (details in Supplement 1, Fig. S9). Both SHG and OCM intensities were normalized. In the color bars for birefringence and SHG-anisotropy parameters, the low (*lo.*) and high (*hi.*) regions represent the 5% and 95% quantiles.

estimated helix angle (θ_H), SHG-anisotropy parameter (ρ), and the corresponding H&E histology image of the same sample (note that FOVs are not exactly matched due to distortions in the fixation and sectioning procedure). The detection spectral bandwidth for τ_{ch1} and τ_{ch2} are 390–506 nm and 506–665 nm, respectively, and the SHG was detected below 390 nm for an excitation beam of 760 nm. All lifetime images were displayed with intensity overlaid and the intensity images can be found in Supplement 1, Fig. S3.

FOV1 was from the dermal-epidermal junction, which was imaged 20 µm deep into the skin. Most of the signals were from cells, which were also seen in the image taken 5 µm closer to the skin surface (Supplement 1, Fig. S4). In FOV1, there were some dermis collagen fibers (star) overlayed on the cells, and a thin lining of the membrane (arrow) was not seen in the SHG channel but seen in 2PFLIM channels and OCM. This membrane structure had a mean phase lifetime of around 1.2 ns. PSHG analyses were not performed because the SHG signals were so low that there were significant random variations in the intensity. FOV2 was 5 µm

deeper from FOV1 and reached inside the dermal layer, showing typical Type I collagen morphology. The lifetime measurement in the lower-wavelength channel (τ_{ch1}) is as low as the SHG response, which is likely due to the strong SHG leaking into the fluorescence channels. FOV2 consists of wavy fibers of various apparent orientations, which is also reflected in the retrieved in-plane angles as seen in the θ_f panel. Distinct fibril structures are visible through both helix angle and anisotropy maps. The estimated helix angle for this dermal collagen has a mean value around 50.5° with 2% CV, and the anisotropy parameter has a mean value around 1.34 with 7% CV. FOV3 was also in the dermis but much deeper (~50 µm) with a hair follicle visualized in the middle of the FOV. Fibrillar collagen was found surrounding the follicle (a layer pointed out by the yellow arrow), as seen by the strong SHG components in the lifetime images. This is known as the connective tissue sheath or the dermal sheath. The inner root sheath (a small circular layer indicated by the white arrow) was also observed, with the cortex in its middle. Both the inner root sheath and the dermal sheath

produced strong SHG. The cortex contains melanin that has a lifetime of around 1.5 ns. Interestingly, the retrieved helix angle distribution has a mean value of 52.7° and 2.5% CV. Upon closer look, the dermal sheath layer and the inner root sheath layer had a helix angle of 53–54°, while the dermal fibers at the outside of the dermal sheath had a helix angle of 51–52°. The basement membrane, which should also be surrounding the follicle, was not obvious in these images due to weaker SHG and autofluorescence signals from type IV collagen. FOV4 was captured 60 µm below the surface, at the location of transition from the dermis (middle to bottom) to the cartilage layer (top). The cartilage in mouse ears is known to have honeycomb structures consisting of type II collagen in which chondrocytes reside [54]. Type II collagen forms a porous structure, which partly accounts for weaker SHG compared to a highly directional structure (such as that in a tendon). Moreover, backscattered SHG signals significantly attenuate in scattering tissue. PSHG analyses of the cartilage area had more noise contributions than the dermal area in the same FOV. We were still able to detect the changes in helix angle that varied from around 50–51° in the dermal area to about 53–54° in the cartilage area. This trend was also observed in the image (Supplement 1, Fig. S5) obtained 10 µm deeper than the FOV4. Besides SHG, we were able to visualize type II collagen via its autofluorescence and through scattering. The mean lifetime of type II collagen in this cartilage was measured to be about 1 ns. The cartilage layer collagen was birefringent but less than the collagen birefringence from the dermal layer. FOV5 was from the hypodermis area where more striated collagen fibers were observed. It was at around 20 µm into the subcutaneous region. The two major fiber bundles in the FOV had relatively high SHG-anisotropy and a mean helix angle at around 50°. These collagen fibers were found together with myosin (Supplement 1, Fig. S6), which was known to have a relatively higher helix angle [35]. In contrast to the collagen in the same FOV, the signal-to-noise ratio (SNR) in SHG intensity of myosin was not enough for quantitative PSHG analyses, but the 2PAF from myosin had a relatively higher intensity than the collagen, with a mean lifetime of about 0.5 ns.

The last row of Fig. 5 compares the major quantitative parameters of the FOVs from five different layers of the rodent outer ears. For both channels, we used bimodal Gaussian fitting to estimate contributions from the different components in the FOVs (Supplement 1, Fig. S7), and we also showed phasor representations of these lifetime distributions in Supplement 1, Fig. S8. The first lifetime channel (Ch1, lower wavelength) was subject to leakage from the SHG channel since they are spectrally adjacent to each other. Therefore, in FOV2 and FOV3, there were several pixels with lifetime values close to 0 ns. However, the τ_{ch2} for FOV2-4 also had a component at around 0.2–0.3 ns, which indicates another low-lifetime autofluorescence component in the tissue. The cartilage in the FOV had both τ_{ch1} and τ_{ch2} to be around 1 ns, which matched well with the fluorescence lifetime of type II collagen gel (Fig. 2).

4. DISCUSSION

From our results for imaging pure collagen gels, it is clear that type I, II, and III are fibrillar whereas type IV is not. Unlike type I, type II, and III fibrils are below the optical resolution, and only the averaged backscattered signals (both OCM and MPM) can be captured. SHG requires non-centrosymmetry at a scale of 200–300 nm, which is apparent in the SEM images for type I

collagen. However, in the SEM images, type III collagen appears to be mesh-like and, therefore, has some extent of centrosymmetry, which yields weaker SHG. Interestingly, OCM was able to capture scattered signals from multiple type III fibrils. However, due to the process of gelation, type III collagen was formed more isotropically in the gel compared to tissues. Since type IV collagen forms into membrane-like structures and does not satisfy the non-centrosymmetry requirement, it cannot generate SHG signals. Comparing the birefringence values of the four types, type I has the highest birefringence. During gelation, we also noticed that the viscosity and scattering of type I collagen gel of the same concentration was the highest overall, which could indicate more directional fiber orientation and more crosslinked gels. In terms of mean lifetime measurement, since we collected both SHG and 2PAF in the same channel to see the relative contribution of SHG in the MPM signals from different types of collagens, we were not able to capture autofluorescence alone from the type I collagen gel since SHG dominated. Even in the case of tissue imaging with spectral filters to separate SHG from 2PAF channels, there was still significant SHG leakage into the fluorescence channel. Future work is needed to solve this challenge, for example, by selectively exciting collagen 2PAF and suppressing SHG by modulating the phase of the exaction beam. We also compared our lifetime measurements to the values reported in Ref. [26] and observed differences in the mean lifetime of type II collagen. However, since lifetime measurements are subject to various external factors, such as pH, temperature, ion concentration, and fluorophore-protein interactions [56], the lifetime values alone are not always reliable in characterizing all collagen subtypes. Combining the proposed three imaging modalities provides a more robust method to distinguish and characterize collagen subtypes.

Although SHG cannot visualize type IV collagen, it is a standard technique for characterizing fibrillar collagen, especially type I. Tendon is known to be a standard biological sample for type I collagen, and the fibers are highly organized. Intuitively, the same piece of tendon imaged at the same depth should have similar molecular characteristics and therefore neither the estimated helix angle nor the SHG-anisotropy (ρ) should have a large variance. Comparing our PSHG numerical model results for tendons with and without incorporating linear birefringence measured by PSOCM, it is clear that the model with birefringence gave distributions of helix angles with much less variance (p-value less than 0.001 in both the student t-test and Kruskal–Wallis test). We also showed that the helix angle is independent of apparent fiber orientation, which means that it could be a metric that is less dependent on the morphological features in the tissue. Compared to a numerical model based on the theoretical organization of collagen molecules and statistics [40,57], the estimated helix angle for aligned fibers should be close to the helix angle for a single helix, which was calculated to be 53° and is close to our results. This was one of the two cases described by the theoretical model [40] with the assumption that all helical molecules formed into straight fibrils, which was considered valid for tendons. Another orientation is called the supercoiled fibril, where the collagen molecules twist along a polar axis with an angle much smaller than the helix angle [40]. Supercoiled fibrils are found to be common in soft tissues [40,57], and dermal collagen fibers are one example. In this case, the estimated helix angle is smaller. A helix angle of 52° was reported in Ref. [40], which is comparable to the collagen observed in the dermal layers of the rodent ears (Fig. 4). In this work, we assumed the fibers are in-plane

with the excitation beam. This is a good approximation for our high-numerical aperture multiphoton imaging, which has inherent optical sectioning with an axial resolution of around 1–2 μm. From the simulation result (Supplement 1, Fig. S10), the off-plane tilt angle of the collagen fibers can cause the overestimation of the anisotropy parameter and therefore the underestimation of the helix angle. However, this tilt angle cannot be directly incorporated into the current Fourier transform method for fast PSHG processing. In this work, the axial component of the excitation light field was ignored, given that a high NA objective and tight focus were used, which could potentially underestimate the anisotropy parameter [37]. While this represented a limitation of this work, it could not readily be mediated given the use of nonlinear imaging in this study. Another limitation of the PSHG numerical model used in this work lies in the off-resonance assumption for the Kleinman symmetry. The presence of 2PAF from collagen indicates that there is a resonant component in the second-order nonlinear polarization, which cannot be easily quantified and separated from the non-resonant counterpart. However, the 2PAF of collagen excited at 760 nm was generally much weaker than the SHG and did not have a polarization response (Supplement 1, Fig. S11). Other than linear birefringence, other factors such as diattenuation and depolarization (i.e., polarization scrambling) could also impede the accuracy of the PSHG numerical model [36]. Diattenuation can be quantified using the current PSOCM method with Jones matrix decomposition, but depolarization requires Mueller matrix computations, which will require more alterations and upgrades to the system configuration [30].

Even though the PSHG numerical model should only depend on the relative intensities at various excitation polarizations, it does have requirements on the image SNR. In a simulation with increasing levels of pure Poisson noise (Supplement 1, Fig. S12), lower SNR caused the loss of fiber structures as well as an increase in the data variance of the PSHG-derived quantities, especially the anisotropy parameter and the helix angle. The signal-to-noise ratio also decreased over imaging depth. In rat tendon, the lifetime estimations for 2PAF ch2 were shown to be stable over 100 μm imaging depth, but ch1 started to display inaccuracy at the depth of 90 μm, which can be mitigated by an increase of excitation power (Supplement 1, Figs. S13 and S14). The PSHG results (with birefringence correction) experienced minor fluctuations across the depth range of 20–100 μm, with the CV below 2% at all depths. The impact of increasing depth on OCM intensity was found not as severe as the nonlinear imaging modalities, and the computed phase retardation displayed an expected pattern across depths for the tendon sample (Supplement 1, Fig. S16). Even though the rat tendon cannot represent all types of biological samples, these results still provide insights into the depth-dependency of the multiparametric measurements shown here. Certainly, the maximum imaging depth should be experimentally determined for a specific tissue type. Image SNR sets practical barriers for accurate PSHG analysis of collagen for type II and III, which generate much weaker signals than type I, and at deeper regions of biological tissues. The basement membrane is only tens of nanometers thick, which is very difficult to locate given the fact that the precision of the sample stage in the z (axial) direction is 100 nm in this system. Performing cross-section imaging may be able to capture the basement membrane underneath the skin. However, sectioning (on fresh or fixed tissue) could potentially destroy the tissue microstructures, and the axial optical resolution is not sufficient to resolve these ultrathin regions of these collagen subtypes.

5. CONCLUSION

In this study, we showed that different subtypes of collagen have different microstructures and optical signatures that could be identified and differentiated using a novel multiparametric multimodal polarization-sensitive imaging platform. By combining PSHG, PSOCM, and 2PFLIM simultaneously, the visualization and characterization of collagen subtypes in biological tissue were possible. A single modality was unable to capture every subtype with high signal values. For instance, it was confirmed that type IV collagen does not produce SHG, and type I generates the strongest SHG, which makes it most suitable for performing polarization-sensitive characterizations. Similarly, the autofluorescence intensity and lifetimes differed for each collagen subtype. With PSOCM, we validated the effect of the nanoscale fiber structure on the backscattered signals. The PP2 multimodal imaging platform could capture each collagen subtype with good signal-to-noise levels in at least one of the imaging modalities. We subsequently showed that including tissue birefringence measured by PSOCM in the PSHG numerical model for collagen improves its accuracy in thick tissue imaging. This eliminates the need for tissue sectioning in PSHG sample preparations and can potentially enable *in vivo* assessment of collagen in tissue microenvironment especially in tumors.

We demonstrated that this label-free multimodal polarization-sensitive imaging system can provide multidimensional and quantitative analyses of collagen in fresh tissues. This multimodal imaging tool can be used for collagen subtype differentiation and study the changes of various label-free optical signatures of collagen for disease diagnosis and treatment. In the future, additional optical signatures of collagen subtypes could be incorporated as well, such as nonlinear Raman microspectroscopy. We aim to further advance our multiparametric analyses and study the changes of the biomolecular, biophysical, and biochemical signatures of collagen over tumor progression using this multimodal approach. We believe this multimodal system has great potential as a powerful and noninvasive tool to provide comprehensive information about collagen and further facilitate our understanding of collagen and the multifaceted roles that various subtypes play in tissues and in states of health and diseases.

Disclosures. A patent has been filed for the fast fluorescence lifetime imaging technique described in this paper by JES, RRI, and SAB. The authors declare that they have no other competing interests.

Data availability. The data and codes that support the findings of this study are available from the corresponding author upon reasonable request and through collaborative investigations.

Supplemental document. See Supplement 1 for supporting content.

REFERENCES

1. C. Frantz, K. M. Stewart, and V. M. Weaver, "The extracellular matrix at a glance," J. Cell Sci. **123**, 4195–4200 (2010).
2. S. Ricard-Blum, "The collagen family," Cold Spring Harb. Perspect. Biol. **3**, a004978 (2011).
3. J. Winkler, A. Abisoye-Ogunniyan, K. J. Metcalf, *et al.*, "Concepts of extracellular matrix remodelling in tumour progression and metastasis," Nat. Commun. **11**, 5120 (2020).
4. A. R. Poole, M. Kobayashi, T. Yasuda, *et al.*, "Type II collagen degradation and its regulation in articular cartilage in osteoarthritis," Ann. Rheum. Dis. **61**, 78ii–ii81 (2002).
5. X. Liu, H. Wu, M. Byrne, *et al.*, "Type III collagen is crucial for collagen I fibrillogenesis and for normal cardiovascular development," Proc. Natl. Acad. Sci. USA **94**, 1852–1856 (1997).
6. A. O. Brightman, B. P. Rajwa, J. E. Sturgis, *et al.*, "Time-lapse confocal reflection microscopy of collagen fibrillogenesis and extracellular matrix assembly in vitro," Biopolymers **54**, 222–234 (2000).
7. C. Mazzotta, F. Hafezi, G. Kymionis, *et al.*, "In vivo confocal microscopy after corneal collagen crosslinking," Ocular Surf. **13**, 298–314 (2015).
8. D. Huang, E. A. Swanson, C. P. Lin, *et al.*, "Optical coherence tomography," Science **254**, 1178–1181 (1991).
9. J. A. Izatt, M. R. Hee, G. M. Owen, *et al.*, "Optical coherence microscopy in scattering media," Opt. Lett. **19**, 590–592 (1994).
10. D. Arifler, I. Pavlova, A. Gillenwater, *et al.*, "Light scattering from collagen fiber networks: micro-optical properties of normal and neoplastic stroma," Biophys. J. **92**, 3260–3274 (2007).
11. L. C. U. Junqueira, G. Bignolas, and R. R. Brentani, "Picrosirius staining plus polarization microscopy, a specific method for collagen detection in tissue sections," Histochem. J. **11**, 447–455 (1979).
12. A. Changoor, N. Tran-Khanh, S. Méthot, *et al.*, "A polarized light microscopy method for accurate and reliable grading of collagen organization in cartilage repair," Osteoarthritis Cartilage **19**, 126–135 (2011).
13. S. L. Jacques, J. C. Ramella-Roman, and K. Lee, "Imaging skin pathology with polarized light," J. Biomed. Opt. **7**, 329–340 (2002).
14. X. Chen, O. Nadiarynkh, S. Plotnikov, *et al.*, "Second harmonic generation microscopy for quantitative analysis of collagen fibrillar structure," Nat. Protoc. **7**, 654–669 (2012).
15. R. M. Williams, W. R. Zipfel, and W. W. Webb, "Interpreting second-harmonic generation images of collagen I fibrils," Biophys. J. **88**, 1377–1386 (2005).
16. W. Mohler, A. C. Millard, and P. J. Campagnola, "Second harmonic generation imaging of endogenous structural proteins," Methods **29**, 97–109 (2003).
17. E. Brown, T. McKee, E. DiTomaso, *et al.*, "Dynamic imaging of collagen and its modulation in tumors in vivo using second-harmonic generation," Nat. Med. **9**, 796–800 (2003).
18. P. P. Provenzano, K. W. Eliceiri, J. M. Campbell, *et al.*, "Collagen reorganization at the tumor-stromal interface facilitates local invasion," BMC Med. **4**, 1–15 (2006).
19. M. W. Conklin, J. C. Eickhoff, K. M. Riching, *et al.*, "Aligned collagen is a prognostic signature for survival in human breast carcinoma," Am. J. Pathol. **178**, 1221–1232 (2011).
20. G. Xi, W. Guo, D. Kang, *et al.*, "Large-scale tumor-associated collagen signatures identify high-risk breast cancer patients," Theranostics **11**, 3229–3243 (2021).
21. S. Huang, A. A. Heikal, and W. W. Webb, "Two-photon fluorescence spectroscopy and microscopy of NAD (P) H and flavoprotein," Biophys. J. **82**, 2811–2825 (2002).
22. Q. Yu and A. A. Heikal, "Two-photon autofluorescence dynamics imaging reveals sensitivity of intracellular NADH concentration and conformation to cell physiology at the single-cell level," J. Photochem. Photobiol. B **95**, 46–57 (2009).
23. S. You, H. Tu, E. J. Chaney, *et al.*, "Intravital imaging by simultaneous label-free autofluorescence-multiharmonic microscopy," Nat. Commun. **9**, 2125 (2018).
24. M. Monici, "Cell and tissue autofluorescence research and diagnostic applications," Biotechnol. Annu. Rev. **11**, 227–256 (2005).
25. V. Lutz, M. Sattler, S. Gallinat, *et al.*, "Impact of collagen crosslinking on the second harmonic generation signal and the fluorescence lifetime of collagen autofluorescence," Skin Res. Technol. **18**, 168–179 (2012).
26. S. Ranjit, A. Dvornikov, M. Stakic, *et al.*, "Imaging fibrosis and separating collagens using second harmonic generation and phasor approach to fluorescence lifetime imaging," Sci. Rep. **5**, 13378 (2015).
27. M. S. Bergholt, A. Serio, and M. B. Albro, "Raman spectroscopy: guiding light for the extracellular matrix," Front. Bioeng. Biotechnol. **7**, 303 (2019).
28. I. Rocha-Mendoza, D. R. Yankelevich, M. Wang, *et al.*, "Sum frequency vibrational spectroscopy: the molecular origins of the optical second-order nonlinearity of collagen," Biophys. J. **93**, 4433–4444 (2007).
29. Y. Han, J. Hsu, N. H. Ge, *et al.*, "Polarization-sensitive sum-frequency generation microscopy of collagen fibers," J. Phys. Chem. B **119**, 3356–3365 (2015).
30. B. Baumann, "Polarization sensitive optical coherence tomography: a review of technology and applications," Appl. Sci. **7**, 474 (2017).
31. W. Drexler, D. Stamper, C. Jesser, *et al.*, "Correlation of collagen organization with polarization sensitive imaging of in vitro cartilage: implications for osteoarthritis," J. Rheumatol. **28**, 1311–1318 (2001).
32. E. J. Marjanovic, V. Sharma, L. Smith, *et al.*, "Polarisation-sensitive optical coherence tomography measurement of retardance in fibrosis, a non-invasive biomarker in patients with systemic sclerosis," Sci. Rep. **12**, 2893 (2022).
33. C. K. Hitzenberger, E. Götzinger, M. Sticker, *et al.*, "Measurement and imaging of birefringence and optic axis orientation by phase resolved polarization sensitive optical coherence tomography," Opt. Express **9**, 780–790 (2001).
34. F. A. South, E. J. Chaney, M. Marjanovic, *et al.*, "Differentiation of ex vivo human breast tissue using polarization-sensitive optical coherence tomography," Biomed. Opt. Express **5**, 3417–3426 (2014).
35. F. Tiaho, G. Recher, and D. Rouède, "Estimation of helical angles of myosin and collagen by second harmonic generation imaging microscopy," Opt. Express **15**, 12286–12295 (2007).
36. I. Gusachenko and M. C. Schanne-Klein, "Numerical simulation of polarization-resolved second-harmonic microscopy in birefringent media," Phys. Rev. A **88**, 053811 (2013).
37. C. Teulon, I. Gusachenko, G. Latour, *et al.*, "Theoretical, numerical and experimental study of geometrical parameters that affect anisotropy measurements in polarization-resolved SHG microscopy," Opt. Express **23**, 9313–9328 (2015).
38. D. Aït-Belkacem, A. Gasecka, F. Munhoz, *et al.*, "Influence of birefringence on polarization resolved nonlinear microscopy and collagen SHG structural imaging," Opt. Express **18**, 14859–14870 (2010).
39. J. C. Mansfield, V. Mandalia, A. Toms, *et al.*, "Collagen reorganization in cartilage under strain probed by polarization sensitive second harmonic generation microscopy," J. R. Soc. Interface **16**, 20180611 (2019).
40. D. Rouède, E. Schaub, J. J. Bellanger, *et al.*, "Determination of extracellular matrix collagen fibril architectures and pathological remodeling by polarization dependent second harmonic microscopy," Sci. Rep. **7**, 12197 (2017).
41. K. R. Campbell, R. Chaudhary, J. M. Handel, *et al.*, "Polarization-resolved second harmonic generation imaging of human ovarian cancer," J. Biomed. Opt. **23**, 066501 (2018).
42. V. Tsafas, E. Gavgiotaki, M. Tzardi, *et al.*, "Polarization-dependent second-harmonic generation for collagen-based differentiation of breast cancer samples," J. Biophoton. **13**, e202000180 (2020).
43. R. Mercatelli, T. Triulzi, F. S. Pavone, *et al.*, "Collagen ultrastructural symmetry and its malignant alterations in human breast cancer revealed by polarization-resolved second-harmonic generation microscopy," J. Biophoton. **13**, e202000159 (2020).
44. I. Amat-Roldan, S. Psilodimitrakopoulos, P. Loza-Alvarez, *et al.*, "Fast image analysis in polarization SHG microscopy," Opt. Express **18**, 17209–17219 (2010).
45. R. R. Iyer, J. E. Sorrells, L. Yang, *et al.*, "Label-free metabolic and structural profiling of dynamic biological samples using multimodal optical microscopy with sensorless adaptive optics," Sci. Rep. **12**, 3438 (2022).
46. L. Yang, J. Park, E. J. Chaney, *et al.*, "Label-free multimodal nonlinear optical imaging of needle biopsy cores for intraoperative cancer diagnosis," J. Biomed. Opt. **27**, 056504 (2022).
47. L. Yang, J. Park, M. Marjanovic, *et al.*, "Intraoperative label-free multimodal nonlinear optical imaging for point-of-procedure cancer diagnostics," IEEE J. Sel. Top. Quantum Electron. **27**, 6801412 (2021).
48. J. E. Sorrells, R. R. Iyer, L. Yang, *et al.*, "Real-time pixelwise phasor analysis for video-rate two-photon fluorescence lifetime imaging microscopy," Biomed. Opt. Express **12**, 4003–4019 (2021).

49. J. E. Sorrells, R. R. Iyer, L. Yang, *et al.*, "Single-photon peak event detection (SPEED): a computational method for fast photon counting in fluorescence lifetime imaging microscopy," Opt. Express **29**, 37759–37775 (2021).

50. J. E. Sorrells, R. R. Iyer, L. Yang, *et al.*, "Computational photon counting using multithreshold peak detection for fast fluorescence lifetime imaging microscopy," ACS Photon. **9**, 2748–2755 (2022).

51. M. A. Digman, V. R. Caiolfa, M. Zamai, *et al.*, "The phasor approach to fluorescence lifetime imaging analysis," Biophys. J. **94**, L14–L16 (2008).

52. W. N. Meigel, S. Gay, and L. L. Weber, "Dermal architecture and collagen type distribution," Arch. Derm. Res. **259**, 1–10 (1977).

53. A. M. Abreu-Velez and M. S. Howard, "Collagen IV in normal skin and in pathological processes," North Am. J. Med. Sci. **4**, 1 (2012).

54. T. J. Yoo and K. Tomoda, "Type II collagen distribution in rodents," Laryngoscope **98**, 1255–1260 (1988).

55. J. H. Barker, F. Hammersen, I. Bondar, *et al.*, "The hairless mouse ear for in vivo studies of skin microcirculation," Plast. Reconstr. Surg. **83**, 948–959 (1989).

56. M. Y. Berezin and S. Achilefu, "Fluorescence lifetime measurements and biological imaging," Chem. Rev. **110**, 2641–2684 (2010).

57. V. Ottani, M. Raspanti, and A. Ruggeri, "Collagen structure and functional implications," Micron **32**, 251–260 (2001).